# Radar-dark impact crater–related parabolas on Venus: Characterization of deposits with Magellan emissivity data

Nataliya V. Bondarenko

Institute of Radiophysics and Electronics, National Academy of Sciences of the Ukraine, Kharkov, Ukraine

Department of Geological Sciences, Brown University, Providence, Rhode Island, USA

James W. Head

Department of Geological Sciences, Brown University, Providence, Rhode Island, USA

Received 2 March 2004; revised 3 June 2004; accepted 20 July 2004; published 11 September 2004.

[1] We have analyzed the radar-dark parabola deposits associated with impact craters on the surface of Venus using the results of the Magellan radio experiments in both passive and active modes. The extent of mantle deposits is found to be much wider than the dark features observed in synthetic aperture radar (SAR) images. Using the emissivity data, we have classified features coinciding with the radar-dark parabolas into four types related to both differences in ejecta deposition styles for craters of different diameters, and stages in the degradation of crater-related deposits. A model for the microwave properties of the mantled surfaces is proposed. Comparison between the distribution of mantle thickness predicted by the model and the previously published independent results based on modeling of the cratering process show good agreement when the loss tangent of the mantle material is assumed to be within the 0.001–0.005 range. This value is similar to that of dry powders of terrestrial and lunar rocks. On the basis of this work we conclude that radar-dark diffuse features due to these mantles can be up to several meters thick if the loss tangent is assumed to be 0.003. Thin deposits (as little as 7 cm thick) are found to be responsible for the deposits seen in the emissivity parabolas but not observed in the SAR images. These results provide a basis for the interpretation of the character and thickness of mantle deposits, their states of degradation, processes associated with their formation and degradation, and guides to their use in establishing stratigraphic relationships and ages of underlying geologic units on Venus. The results will also be useful in interpreting the nature of surface deposits at previous landing sites and predicting the nature of deposits likely to be encountered at future landing sites. *INDEX TERMS:* 6295 Planetology: Solar System Objects: Venus; 5464 Planetology: Solid Surface Planets: Remote sensing; 5470 Planetology: Solid Surface Planets: Surface materials and properties; *KEYWORDS:* crater-related parabola, emissivity, Venus surface

**Citation:** Bondarenko, N. V., and J. W. Head (2004), Radar-dark impact crater–related parabolas on Venus: Characterization of deposits with Magellan emissivity data, *J. Geophys. Res.*, *109*, E09004, doi:10.1029/2004JE002256.

## 1. Introduction

[2] About 43% of the impact craters on Venus with diameters >22.6 km are associated with distinctive radar-dark diffuse features (DDF) [*Herrick and Phillips*, 1994]. The DDF include west-opening radar-dark parabolas (8%) and radar-dark halos surrounding impact craters (35%). A recent study of DDF [*Basilevsky and Head*, 2002a] provided revised proportions of craters with diameters >30 km with dark parabolas and dark halos as 13.9% and 29.4%, respectively. *Basilevsky and Head* [2002a] extended the crater DDF family by describing the so-called faint dark halo features that are not as distinctly seen or are large but clearly associated with craters. Such features were identified in 21.4% of the crater population [*Basilevsky and Head*, 2002a], and on this basis the total fraction of craters >30 km in diameter with DDF increased to 64.7%.

[3] No significant differences have been found between the distributions of the DDF types for craters of different diameters and in different surface provinces [*Basilevsky and Head*, 2002a]. Differences are seen only in distribution as a function of latitude. There are fewer dark parabola and dark halo craters and more craters with faint dark halos and craters without radar dark deposits in the high-latitude zones (above 37° latitude) compared to the lower latitudes


0148-0227/04/2004JE002256$09.00

[*Basilevsky and Head*, 2002a]. This dependence may be caused by differences in the Magellan synthetic aperture radar (SAR)'s viewing geometry with latitude.

[4] DDFs occupy the highest (uppermost) stratigraphic position relative to their surroundings [*Campbell et al.*, 1992] and thus are among the youngest features and geological units on the Venus surface [e.g., *Basilevsky and Head*, 1995]. Hence craters with DDFs are thought to be the youngest on the planet [*Herrick and Phillips*, 1994; *Campbell et al.*, 1992; *Arvidson et al.*, 1992; *Basilevsky and Head*, 1998, 2000; *Basilevsky et al.*, 2003]. The different DDF types mentioned above are interpreted to represent different stages of degradation for the features in general [*Izenberg et al.*, 1994; *Basilevsky and Head*, 2002b]. The sequence from dark parabola through dark halo to faint dark halo is interpreted to represent their relative age and a trend of increasing age [*Basilevsky and Head*, 2000; *Basilevsky et al.*, 2003]. Thus the distribution and characteristics of DDFs can potentially be a useful tool for the study of geological processes on the surface of Venus with time. The morphological degradation stages of the DDF have been used for the study of tectonic activity [*Izenberg et al.*, 1994], and for the dating of geological units and features on Venus [*Basilevsky and Head*, 2002b].

[5] DDFs were initially interpreted to be surficial deposits of loose material (e.g., dust) formed by impacts [*Campbell et al.*, 1992]. The unusual parabolic shapes, with west-facing dark parabolas, are explained by the influence on the material lifted by impacts of the westward zonal winds in the atmosphere [*Vervack and Melosh*, 1992; *Campbell et al.*, 1992]. Dark diffuse features change their shapes with geological time and disappear due to aeolian activity [e.g., *Greeley et al.*, 1992], which moves the dust and scatters it over larger areas, and/or due to some weathering processes [e.g., *Wood*, 1997]. Aeolian features observed in Magellan SAR images [*Arvidson et al.*, 1992] also support the presence of loose material moveable by winds on the surface. Direct observations of loose material on the surface of Venus were made during the Venera 9, 10, 13, and 14 missions [*Florensky et al.*, 1977; *Basilevsky et al.*, 1985]. There is a significant amount of fine material seen in the Venera 9 and Venera 13 panoramas. In the Venera 10 and Venera 14 landing sites loose material was observed in discontinuous shallow depressions [*Florensky et al.*, 1977; *Basilevsky et al.*, 1985]. The lack of loose material in the narrow zone close to the Venera 13 lander was interpreted to be caused by the blowing away of fines induced by turbulence during landing. These observations indicate that the observed dark material is loose and moveable by airflow.

[6] On the basis of these observations, we consider crater-related DDFs on Venus as mantles covering the substrate. In this paper we use the results of active and passive microwave probing of the surface of Venus with instruments on board the Magellan spacecraft to analyze the microwave properties of DDF material, the extent of DDF-related deposits, and the influence of viewing geometry on the detection of the deposits. We propose a model for calculation of the microwave properties of the mantled surface and deposits. We then use the model to estimate mantle depths, and thus the thicknesses of the deposits. We then discuss the appropriate choice of loss tangent for the mantle material and summarize observations on the characteristics of the thin mantles.

## 2. DDF in the Radar Cross-Section–Emissivity Domain

[7] Two complementary Magellan data sets are used in this study. The first one is the side-looking radar backscatter cross-section images obtained with the synthetic aperture radar (SAR) in the active mode. The second data set is the emissivity derived from radiometric (passive mode) measurements with the same antenna. Both data sets were obtained at a wavelength of 12.6 cm and with the same viewing geometry. The spatial resolution of the emissivity measurements is about 20 km at periapsis (9.5°N latitude) [*Plaut*, 1993]. SAR data spatial resolution was on the order of 100 m at low latitudes [*Ford and Plaut*, 1993]. We reduced the resolution of the SAR data to make them comparable with the resolution of the emissivity data. In the present study we used the emissivity and SAR data mostly from the first cycle of the Magellan mission. C1-MIDR mosaics were used as a source of radar cross section, and emissivity maps (GEDR data set) provided the emissivity values.

### 2.1. Classification of Emissivity Features Observed for Radar-Dark Parabolas

[8] Features interpreted as extended crater-related deposits were found not only in SAR images but also in emissivity maps. *Campbell et al.* [1992] reported eight dark emissivity features characterized by parabolic shapes generally open to the west. The typical difference in emissivity between parabolas and the surrounding plains is about 0.05 [*Campbell et al.*, 1992]. Six parabolas are located in Guinevere and Tinatin planitiae [*Arvidson et al.*, 1991]. The majority of emissivity parabolic features coincide with the barely discernible parabolic-shaped features in SAR images. For example, in the case of the 37.6 km diameter crater Carson (−24.2°N, 344.1°E) the parabolic feature is clearly seen in both SAR and emissivity images. In the case of the 10.8 km diameter unnamed crater at 0.9°N, 338°E, only the south part of emissivity parabola is seen in SAR image as a dark area [*Campbell et al.*, 1992]. All emissivity features listed by *Campbell et al.* [1992] are related to craters with diameters less then 21 km.

[9] We examined emissivity features seen in the emissivity map in the same locations as the radar-dark parabolas for craters within the latitude zone extending from 66°S–66°N. At higher latitudes the resolution of the emissivity data is too poor (>50 km) to be useful. Craters with DDF as listed by *Campbell et al.* [1992] and *Basilevsky and Head* [2000] were used for this analysis. These lists were supplemented by craters having emissivity parabolas exhibited in SAR images as partly parabolic shapes or those not exhibiting any radar-dark features [*Campbell et al.*, 1992]. Four craters with dark emissivity and/or radar parabolas were found using data from the second Magellan cycle which covered gaps of the first cycle of radar mapping. The crater set under analysis was also extended to include seven new craters with small diameters showing roughly parabolic emissivity features not previously reported.

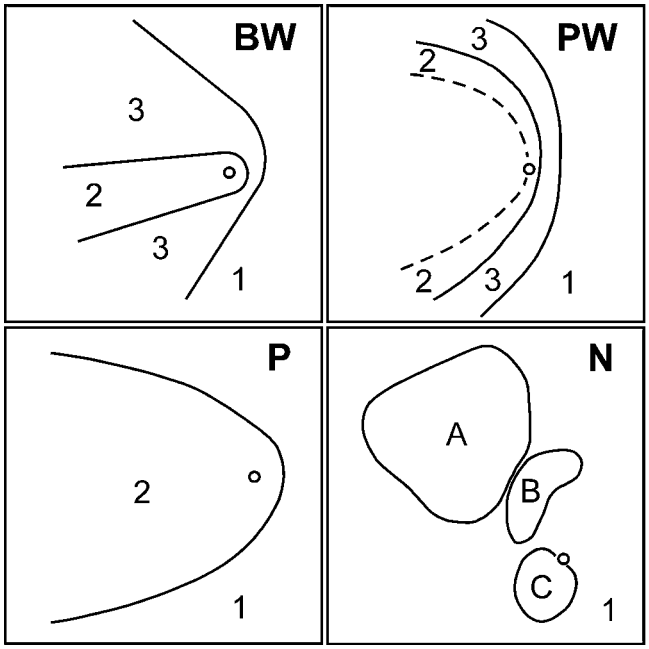


**Figure 1.** Sketches for four types of emissivity appearances for craters with radar-dark parabolas. Small circles denote crater locations. 1, surrounding surface; 2, low emissivity; 3, high emissivity. For N type, A, B, and C are recognized emissivity features of some emissivity values within DDF (crater Comnena, Figure 7, was used as a prototype).

[10] This analysis showed that radar-dark parabolas observed in SAR images can exhibit either lower or higher emissivity than their surroundings, or can not show any differences from their surroundings in the emissivity map. Sometimes radar-dark parabolas maintain a roughly parabolic shape in the emissivity maps, but often only parts of parabolas are seen or no distinctive parabolic shapes can be seen at all.

[11] We subdivided all analyzed emissivity features into four types according to their general appearance (see sketches in Figure 1). The first subgroup (designated BW type for their black and white appearance) contains 11 craters (Table 1). These are characterized by associated emissivity features that have a lower-emissivity inner part and a higher-emissivity outer part (Figure 1). An example of such a feature related to the 22.4 km diameter crater Faustina (22.1°N, 4.7°E) is seen in Figure 2. The location of the crater in the SAR (Figure 2b) and emissivity (Figure 2a) images is marked by arrows. The high-emissivity area has a rather distinctive eastern boundary and has an approximately parabolic shape. The width of this area is about 360 km for the section marked as AB in Figure 2a. The high-emissivity area in the inner part coincides with the radar-dark parabola and thus as a whole represents extended crater deposits. For four of the BW craters from Table 1 (Boulanger, Yablochkina, Stowe, and Sabin), the eastern boundary of the high-emissivity features are poorly delineated. This may arise from the complex geologic environment, the lower resolution of the emissivity data (some of these craters are at rather high latitudes), or other unknown reasons.

[12] A second subgroup of emissivity features (designated PW-type for parabola-white, see Figure 1) contains six craters (Table 1). These emissivity features look like high-emissivity parabolas enclosing low-emissivity parabolas. The inner parts of high-emissivity parabolas coincide with radar-dark parabolas seen in SAR images. Thus the high-emissivity parabolas may be caused by extended crater deposits similar to the BW type but much narrower. Some low-emissivity areas can be observed in the inner or western part of the radar parabola. A PW feature is observed related to the 32.8 km diameter crater Sitwell (16.64°N, 190.4°E) shown in Figure 3. Arrows show the locations of the crater in the emissivity and radar images (Figures 3a and 2b, respectively). The radar-dark parabola in the SAR image coincides partly with the low, and partly with the high-emissivity parabolas. The width of the emissivity parabola in the lower part of Figure 3a between A and B is about 160 km. An emissivity parabola associated with crater Adaiah (see Table 1) has a much more complex structure.

[13] All BW and PW craters listed in Table 1 are accompanied by median emissivity values for the low- and high-emissivity parts of the features and for the surrounding surface. Also the median radar cross-section deficiencies between the darkest areas in the SAR parabolas and pure surrounding plains are shown; apparent tectonic and other obviously roughness-related features were excluded from the analysis. The difference varies from ~13 dB to 4 dB and reaches higher values for BW craters.

[14] A third subgroup of emissivity feature (designated P-type emissivity features for pure dark emissivity parabolas; see Figure 1) contains twenty-four craters (Table 2). Some of these coincide with distinctive SAR parabolic features, but many others are not associated with any dark diffuse features in SAR images. The 22.4 km diameter crater Li Quingzhao (23.7°N, 94.6°E; Figure 4) and the 18.8 km diameter crater Nadine (7.8°N, 359.1°E; Figure 5) are examples of these two situations, respectively. Difference in emissivity between the parabolas and the surrounding plains for these craters is about 0.05. The widths of the emissivity features at sections AB in Figure 4a and Figure 5a are 550 km and 180 km, respectively.

[15] Three unnamed craters (bottom of Table 2) have wind-streak-like extended deposits in SAR images. In the emissivity map at the same locations rather narrow but symmetric features are observed, as they are for the unnamed 5.8 km diameter crater at 1.3°S, 156.5°E (Figure 6a). The western part of the emissivity feature is about 140 km wide (AB in Figure 6a) and differs from the surrounding surface by 0.05. Two other unnamed craters represent the smallest in the data set (with diameters of 2.8 km and 5.1 km). The small crater size corresponds to lower initial ejecta velocity and shorter ejecta ballistic distance [*Melosh*, 1989]. The latter is likely to be the reason for the formation of narrow deposits.

[16] Differences in radar cross section between the darkest values in areas associated with deposit and their features and the pure adjacent surface are shown in Table 2. Higher differences usually occur for craters with well recognized radar-dark parabolas. The diameters of craters associated with P-type emissivity parabolas are never greater then 28 km.

[17] A fourth subgroup of emissivity feature (designated N-type emissivity features for the lack of, or no dark

**Table 1.** Bimodal Emissivity Features for Radar-Dark Parabolas[a]

| Crater Name | Lat. | Long. | D, km | θ, ° | Emissivity | | | Δσ, dB |
|---|---|---|---|---|---|---|---|---|
| | | | | | Low | High | Plains | |
| *Solid Black and White (BW) Emissivity Features* | | | | | | | | |
| Greenaway | 22.9° | 145.1° | 92.3 | 44.15° | 0.801 | 0.844 | 0.828 | 6.8 |
| Stowe | −43.2° | 233.2° | 80.0 | 25.93° | 0.800 | 0.844 | 0.830 | 8.0 |
| Boulanger | −26.6° | 99.3° | 71.5 | 34.62° | 0.798 | 0.870 | 0.845 | 9.8 |
| Boleyn | 24.4° | 220.1° | 70.4 | 43.76° | 0.801 | 0.861 | 0.825 | 11.8 |
| Stuart | −30.8° | 20.2° | 68.6 | 32.37° | 0.814 | 0.855 | 0.848 | 8.8 |
| Yablochkina | 48.3° | 195.3° | 64.3 | 34.18° | 0.811 | 0.851 | 0.864 | 7.2 |
| Ban Zhao | 17.0° | 146.9° | 38.3 | 45.26° | 0.817 | 0.844 | 0.824 | 12.8 |
| Himiko | 19.0° | 124.3° | 36.7 | 44.98° | 0.803 | 0.855 | 0.834 | 12.6 |
| Sabin | −38.5° | 274.7° | 33.1 | 28.26° | 0.813 | 0.877 | 0.853 | 11.6 |
| Adivar | 8.9° | 76.2° | 30.3 | 45.71° | 0.771 | 0.803 | 0.827 | 8.0 |
| Faustina | 22.1° | 4.7° | 22.4 | 44.35° | 0.812 | 0.886 | 0.848 | 10.6 |
| *Emissivity Features With Thin White Parabola (PW)* | | | | | | | | |
| Carson | −24.2° | 344.1° | 37.6 | 35.93° | 0.786 | 0.852 | 0.833 | 10.2 |
| Sitwell | 16.6° | 190.4° | 32.8 | 45.33° | 0.848 | 0.876 | 0.845 | 9.2 |
| Von Schuurman | −5.0° | 191.0° | 28.9 | 43.80° | 0.776 | 0.828 | 0.835 | 8.0 |
| Ruth | 43.3° | 19.9° | 17.9 | 36.60° | 0.817 | 0.849 | 0.84 | 6.8 |
| Adaiah | −47.3° | 253.4° | 17.5 | 24.12° | 0.800 | 0.882 | 0.843 | 6.0 |
| unnamed | 10.6° | 346.3° | 12.8 | 45.69° | 0.780 | 0.838 | 0.823 | 4.0 |

[a]"Low," the median emissivity over low-emissivity feature; "High," the median emissivity over high-emissivity feature; "Plains," the median emissivity over the plains area recognized as pure surface nearby; Δσ, the difference in radar cross section between the darkest values inside SAR parabola and pure plains nearby; "Lat.," latitude; "Long.," east longitude; θ, incidence angle for both SAR and radiometry observations, "D," crater diameter in kilometers.

parabolic features) contains eighteen craters (Table 3). The surface covered by SAR parabolas can show some emissivity variations that do not form a parabolic feature or do not differ from the surroundings. In Figure 7, radar-dark deposits for the 19.0 km diameter crater Comnena (1.2°S, 343.7°E) are seen in the emissivity map (Figure 7a) as three areas (see Figure 1). The lowest emissivity feature here is located inside the radar-dark halo surrounding the crater. The large high-emissivity area (the 250 km between A and B marks in Figure 7a) is characterized by wide wind streaks in the western part of the radar parabola. Similar emissivity structures are observed for craters in a wide range of diameters (Table 3).

[18] The diversity of radar cross-section–emissivity structures for dark parabolic deposits underlines the unusual and variable properties of impacts and/or to the degradation of the material of the mantle itself. The small size of the total population of craters makes a statistical approach to analysis unreliable. In some ways, every impact on Venus surface is a rather unique event [e.g., *Schultz*, 1992]. The differences in crater diameters translate into differences in ejecta volumes and penetration depths. Furthermore, the impact can occur on surfaces and substrates of different types and can excavate material with different properties from the same depth. Thus contributions to the observed radar properties from the variety of surfaces and mantles can cause highly diverse SAR and emissivity signatures for extended crater deposits.

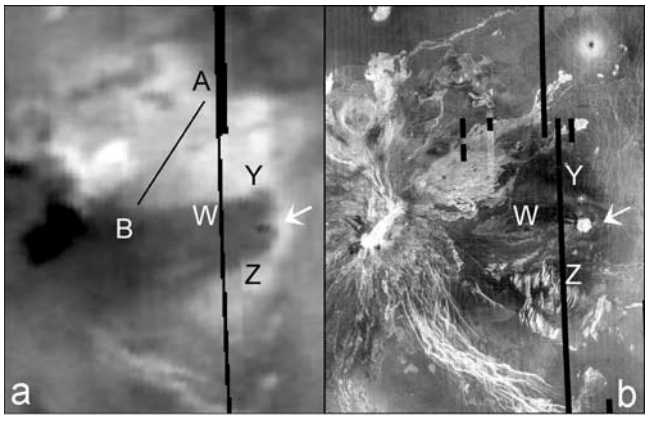


**Figure 2.** Emissivity feature of the BW type and a radar-dark parabola associated with crater Faustina, (22.1°N, 4.7°E, 22.4 km). (a) Emissivity map. Here and in all other emissivity maps the brighter shades denote higher emissivity values. The length of segment AB is 360 km. (b) SAR image. Here and in all other maps and images the double arrows point to the crater itself.

### 2.2. Radar Cross-Section–Emissivity Diagrams for Dark Diffuse Features

[19] A typical emissivity–radar cross-section diagram, or scatterplot, for a DDF is shown in Figure 8d. Each pixel represents the normalized surface area with a specific emissivity and radar cross section. The 68.6 km diameter crater Stuart (30.79°S, 20.22°E) was used as an example for

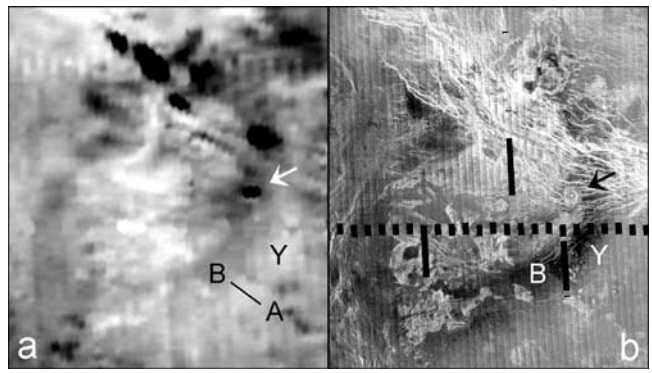


**Figure 3.** Emissivity feature of the PW type associated with the crater Sitwell (16.64°N, 190.4°E, 32.8 km). (a) Emissivity map. The length of segment AB is 160 km. (b) SAR image.

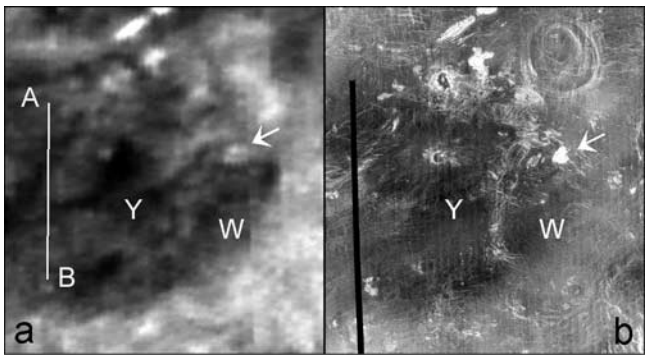


**Figure 4.** Emissivity feature of the P type associated with the crater Li Quingzhao (23.7°N, 94.6°E, 22.4 km). (a) Emissivity map. The length of segment AB is 550 km. (b) SAR image; radar-dark parabola is seen.

this diagram. Emissivity and SAR images of the crater are shown in Figures 8a and 8b, respectively. The crater Stuart has a BW type emissivity structure. In the diagram (Figure 8d) the radar cross section ($\sigma$) is plotted along the horizontal axis and emissivity ($E$) along the vertical axis. The floor of the crater is excluded because of its extremely low emissivity (<0.73).

[20] DDF are usually recognized in SAR images on the basis of their lower radar cross section. In Figure 8c the surface surrounding the crater Stuart is classified according to the value of the radar cross section. In the diagram (Figure 8d) the separation is marked with a vertical line. The part of the diagram to the left of the line corresponds to the apparent DDF and right part of the diagram to the apparent surroundings.

[21] Analysis of the dark diffuse features in diagrams similar to that in Figure 8d permitted the derivation of some general properties of the emissivity behavior for these features. The emissivity of the DDFs, excluding the craters themselves, is usually within the range of the typical emissivity of the surrounding surfaces. Minimal values of DDF emissivity are generally higher than that for the surroundings. For the crater Stuart (see Figure 8d) it is higher by 0.04. Only for the 36.7 km diameter crater Himiko (19°N, 124.3°E) the minimal DDF emissivity is lower, by 0.09. These observations, in general, point to lower values of dielectric permittivity for the mantle and are consistent with the mantle being formed by loose material.

[22] The range of emissivity for the DDF (see, for example, Figure 8d) is narrower in comparison to that of the surrounding surface. Similar relationships were observed for all of the DDF analyzed. Thus we conclude that the mantled surfaces are smoother, and the material forming the DDF is more homogeneous in comparison with the diversity of the nearby surfaces.

[23] Emissivity features for extended crater deposits were recognized using visual analysis. These features are usually rather large. The widths of emissivity features shown in Figures 2–7 (denoted by the AB lines) vary from 140–550 km, values much larger than the resolution of the emissivity data. Along every feature the emissivity maintains almost the same value within formal errors (±0.01). In the SAR images, in the context of the extent of the emissivity features, the radar brightness often changes gradually (Figures 2–7). This situation can be shown in detail for the 38.3 km diameter crater Ban Zhao (17.2°N, 146.9°E) shown in Figure 9. The crater is located in a large crater field and has a distinctive emissivity feature of the BW type. The eastern boundary of the high-emissivity parabola is marked with dashed lines in both emissivity (Figure 9a) and SAR (Figure 9b) images. This boundary crosses several lava flows and lava plains units (for example, S and G) and no geological boundaries are seen at the same positions in the emissivity image. The inner part of the higher-emissivity parabola coincides with the radar-dark parabola and hence is related to the crater ejecta. The outer part of the emissivity parabola is outside the DDF seen in the SAR image. Thus crater-related mantling deposits have a wider extent in the emissivity image in comparison to the dark areas seen in SAR images. The section through the high-emissivity parabola (shown with dots in Figure 9a) permits the tracing of the relationship between emissivity and radar cross section in the diagram in Figure 10. The change in radar brightness along the section is about 10 dB while at the same time emissivity maintains almost constant values.

[24] Features of constant emissivity and a coincident gradual change in radar brightness were observed for all dark parabola craters listed by *Campbell et al.* [1992] and *Basilevsky and Head* [2002a]. Similar features are seen for 20 of 39 dark-halo craters and for 18 of 31 faint-dark-halo craters in the diameter range 30–80 km from the work by *Basilevsky and Head* [2002a]. In conclusion, this relationship between similar emissivity and a gradual change of radar cross section is typical for surfaces influenced by extended impact crater deposits on Venus.

## 3. A Model for the Microwave Properties of the Mantled Surface

[25] Observations described in the previous section permit the specification of several of the general properties of the mantled surfaces. The mantle is formed by loose material produced during impact. The mantle influences

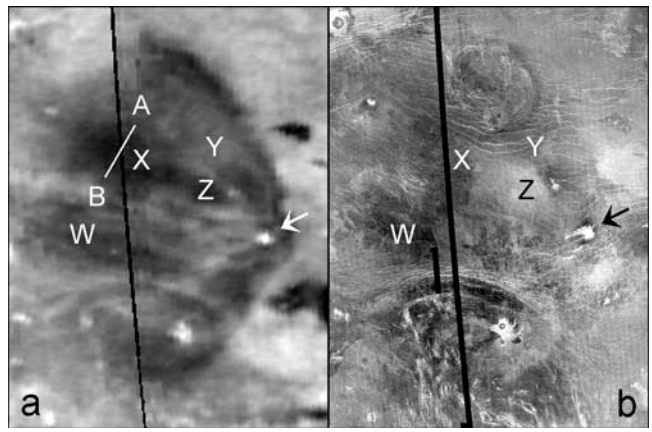


**Figure 5.** Emissivity feature of the P type associated with the crater Nadine (7.8°N, 359.1°E, 18.8 km). (a) Emissivity map. The length of segment AB is 180 km. (b) SAR image; no distinctive parabolic feature is seen.

**Table 2.** Parabolic Emissivity Features[a]

| Crater Name | Latitude | Longitude | D, km | θ, ° | Emissivity | | Δσ, dB |
|---|---|---|---|---|---|---|---|
| | | | | | Low | Plains | |
| Glaspell | −58.5° | 269.6° | 27.7 | 20.79° | 0.849 | 0.861 | 5.4 |
| Eudocia | −59.1° | 202.0° | 25.9 | 20.67° | 0.813 | 0.828 | 2.6 |
| Akeley | 8.0° | 244.5° | 22.7 | 45.71° | 0.763 | 0.827 | 9.2 |
| Frank | −13.1° | 12.9° | 22.6 | 41.17° | 0.725 | 0.826 | 8.4 |
| Abington | −47.8° | 277.7° | 22.6 | 23.92° | 0.824 | 0.856 | 7.0 |
| Li Quingzhao | 23.7° | 94.6° | 22.4 | 43.95° | 0.783 | 0.822 | 9.2 |
| Anaxandra | 44.2° | 162.3° | 20.2 | 36.18° | 0.819 | 0.846 | 5.2 |
| Rowena | 10.4° | 171.4° | 19.6 | 45.69° | 0.827 | 0.766 | 4.0 |
| du Chatelet | 21.5° | 165.0° | 19.0 | 44.48° | 0.782 | 0.84 | 9.2 |
| Nadine | 7.8° | 359.1° | 18.8 | 45.71° | 0.778 | 0.833 | 6.8 |
| Noreen | 33.6° | 22.7° | 18.2 | 40.85° | 0.779 | 0.827 | 10.2 |
| Merit Ptah | 11.4° | 115.6° | 17.0 | 45.68° | 0.827 | 0.844 | 11.8 |
| Vashti | −6.8° | 43.7° | 16.5 | 24.89° | 0.824 | 0.841 | 7.2 |
| Miriam | 36.5° | 48.2° | 15.5 | 25.1° | 0.755 | 0.826 | 7.6 |
| unnamed | −40.7° | 151.9° | 14.9 | 27.15° | 0.834 | 0.861 | 5.2 |
| Rose | −35.2° | 248.2° | 14.7 | 29.99° | 0.774 | 0.843 | 7.6 |
| Gillian | −15.2° | 50.1° | 14.3 | 25.01° | 0.804 | 0.839 | 9.4 |
| unnamed | 24.3° | 253.0° | 13.0 | 43.79° | 0.74 | 0.823 | 3.2 |
| Lyon | −66.5° | 270.5° | 11.6 | 19.41° | 0.844 | 0.868 | 4.6 |
| unnamed | 0.9° | 338.7° | 10.8 | 45.06° | 0.762 | 0.83 | 4.4 |
| unnamed | −62.4° | 33.8° | 10.1 | 20.11° | 0.847 | 0.852 | 3.8 |
| unnamed | 2.9° | 5.0° | 9.4 | 45.37° | 0.762 | 0.825 | 4.0 |
| unnamed | 66.1° | 178.0° | 6.7 | 25.52° | 0.825 | 0.855 | 3.2 |
| unnamed | 21.9° | 37.2° | 6.4 | 24.94° | 0.783 | 0.828 | 3.4 |
| unnamed | −1.3° | 156.5° | 5.8 | 44.65° | 0.774 | 0.849 | 6.8 |
| unnamed | 7.3° | 282.0° | 5.1 | 45.7° | 0.776 | 0.829 | 5.2 |
| unnamed | −23.0° | 150.9° | 2.8 | 36.56° | 0.835 | 0.854 | 5.0 |

[a]See Table 1 notes for "Low," "Plains," and Δσ descriptions.

the observed microwave properties of surfaces that it mantles. It causes uniform emissivity over large areas and a gradually changing radar cross section. The mantled surface looks more homogeneous and smoother in comparison with the apparently unmantled surfaces nearby.

[26] As a first approximation, a mantle can be considered as a layer of homogeneous material. The darkening of observed radar brightness is considered to occur due to the attenuation of radio waves in the mantle itself. This approach has been used for estimation of the dune size [e.g., *Arvidson et al.*, 1992], as well as for some mantle depth estimations [e.g., *Campbell et al.*, 1992].

### 3.1. Model Formulation

[27] The properties of extended deposits from impacts were studied with a simple model of surface structure as a half-space of material with dielectric permittivity $\varepsilon_1$ representing the substrate covered by the mantle with dielectric permittivity $\varepsilon_2$ (Figure 11). The atmosphere-mantle interface was considered to be flat. We used this approximation taking into account, that according to the work by *Schaller and Melosh* [1998], the top of the deposits responsible for DDF is formed by small particles, for example, 200–1000 μm for craters of 10–40 km in diameter. On the other hand, craters with parabolic DDF are considered to be the youngest on the planet [*Herrick and Phillips*, 1994; *Campbell et al.*, 1992; *Arvidson et al.*, 1992; *Basilevsky and Head*, 1998, 2000; *Basilevsky et al.*, 2003]. Hence it is reasonable to suggest that wind-caused particle movement has not yet made the interface rough at the Magellan wavelength. Recently reported work by *Carter et al.* [2004] showed independent evidence for a smooth upper mantle interface at a scale of 12.6 cm.

[28] Interaction between the incident radiation and the surface of the structure shown in Figure 11 can be described in the following way. First, the radiation is partly reflected at the upper flat interface and partly transmitted into the mantle. The angle of refraction for the transmitted radiation θ′ (see Figure 11) can be calculated by Snell's law [e.g., *Born and Wolf*, 1964; *Stratton*, 1947]. The intensity of

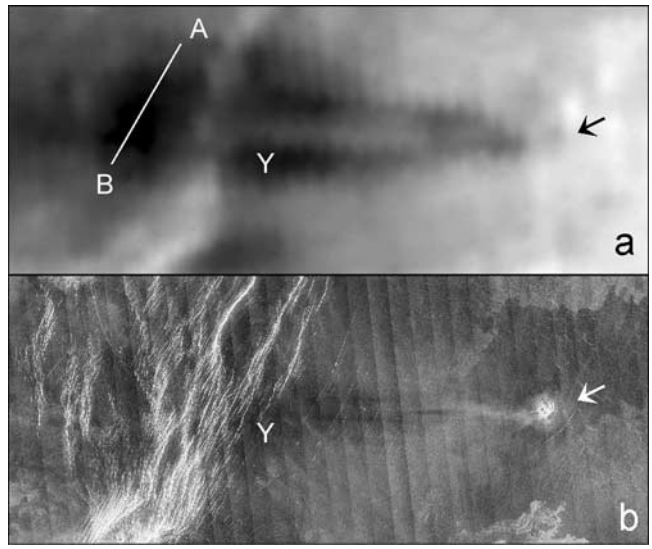


**Figure 6.** Emissivity feature of the P type associated with an unnamed crater at 1.3°S, 156.5°E (5.8 km). (a) Emissivity map. The emissivity parabola is narrow; segment AB is 140 km long. (b) SAR image; the crater shows weak radar structures similar to wind streaks.

**Table 3.** Nonparabolic Emissivity Appearances for Radar-Dark Parabolas[a]

| Crater Name | Latitude | Longitude | D, km | θ, ° | Emissivity | | Δσ, dB |
|---|---|---|---|---|---|---|---|
| | | | | | SAR Parabola | Plains | |
| Caldwell | 23.7° | 112.4° | 51.0 | 43.97° | 0.803–0.818 | 0.837 | 13.4 |
| Austen | −25.0° | 168.5° | 43.9 | 35.50° | 0.812–0.836 | 0.859 | 5.8 |
| Guan Daosheng | −61.1° | 181.8° | 43.0 | 20.32° | 0.816–0.829 | 0.824 | 2.8 |
| Montesori | 59.4° | 280.0° | 42.9 | 28.59° | 0.829–0.862 | 0.851 | 7.4 |
| Uvaysi | 2.3° | 198.2° | 38.0 | 45.29° | 0.825–0.871 | 0.859 | 5.0 |
| Aurelia | 20.3° | 331.8° | 31.1 | 44.75° | 0.818–0.835 | 0.842 | 8.0 |
| Bassi | −19.0° | 64.7° | 31.0 | 38.61° | 0.814–0.852 | 0.845 | 8.2 |
| Magnani | 58.6° | 337.2° | 26.6 | 28.99° | 0.845–0.894 | 0.864 | 5.6 |
| Holiday | −46.7° | 12.9° | 26.3 | 24.37° | 0.851–0.866 | 0.876 | 6.0 |
| Martinez | −11.7° | 174.7° | 23.1 | 41.70° | 0.848–0.854 | 0.867 | 10.0 |
| Comnena | 1.2° | 343.7° | 19.0 | 45.11° | 0.826–0.837 | 0.821 | 7.4 |
| Cohn | −33.3° | 208.1° | 18.7 | 31.01° | 0.818–0.840 | 0.856 | 6.6 |
| Francesca | −28.0° | 57.7° | 17.1 | 25.01° | 0.839–0.844 | 0.848 | 6.1 |
| Akiko | 30.6° | 187.3° | 17.1 | 41.90° | 0.864 | 0.869 | 6.2 |
| Audrey | 23.8° | 348.1° | 15.3 | 43.92° | 0.824–0.813 | 0.826 | 7.0 |
| unnamed | −9.3° | 157.0° | 11.8 | 42.53° | 0.849–0.862 | 0.869 | 4.2 |
| unnamed | 37.2° | 207.9° | 11.2 | 39.36° | 0.828–0.846 | 0.850 | 9.0 |
| Phyllis | 12.2° | 132.4° | 10.6 | 45.65° | 0.838–0.848 | 0.846 | 8.8 |

[a]See Table 1 notes for "Plains" and Δσ descriptions.

transmitted radiation is reduced in comparison with the incident flux one by a factor of $B(\varepsilon_2, \theta) = 1 - R(\varepsilon_2, \theta)^2$, where $R(\varepsilon, \theta)$ is the Fresnel reflection coefficient. An analogous change in ray direction and intensity occurs at the upper interface, when the radiation leaves the mantle. The coefficient in this case is $B(1/\varepsilon_2, \theta')$, $B(\varepsilon, \theta)$ being defined above. Inside the mantle, the radiation is absorbed by mantle material while traveling from the upper interface to the substrate and back. Attenuation of the radiation is

$$A(\varepsilon_2, \tan\Delta, H, \theta') = \exp(-4\pi \cdot \tan\Delta \cdot \sqrt{\varepsilon_2} \cdot H / \cos\theta' \cdot \lambda), \quad (1)$$

where $\lambda$ is the wavelength, $\tan\Delta$ and $\varepsilon_2$ are the loss tangent and dielectric permittivity of the mantle material, respectively, and $H$ is the thickness of the mantle. When the radiation reaches the mantle - substrate interface, it is scattered. The scattering coefficient $S(\varepsilon_{12}, \xi, \theta')$ depends on the relative dielectric permittivity of $\varepsilon_{12} = \varepsilon_1/\varepsilon_2$, the incidence angle $\theta'$ of radiation, and substrate roughness, which we describe with a parameter $\xi$ (see below).

[29] Thus the backscattering coefficient for the model (Figure 11) with the definitions described above can be presented as

$$\sigma(\theta) = S(\varepsilon_{12}, \xi, \theta') \cdot A(\varepsilon_2, \theta', \tan\Delta, H) \cdot B(\varepsilon_2, \theta) \cdot B\left(\frac{1}{\varepsilon_2}, \theta'\right). \quad (2)$$

[30] The path of the backscattered wave is marked with a solid line in Figure 11. The model does not consider multiple reflect of the radiation between interfaces inside the mantle; estimations show that its contribution is small enough to be neglected. The model also does not take into account interference effects; for the mantle of appreciable thickness (compared to the wavelength) these effects could average out due to the inevitable variations in the mantle thickness.

[31] Thus the presence of a mantle affects wave scattering through the attenuation of radiation during its passage through the mantle, the change of angle of incidence radiation reaching the lower mantle-substrate interface, and through the change of scattering coefficient.

[32] Emissivity was calculated using Kirchhoff's law, which states that under thermal equilibrium emissivity of the medium is equal to the fraction of radiation that is absorbed by the medium. Emissivity at the angle $\theta$ was calculated through the reflectivity $\Gamma(\theta)$ of the surface at incidence angle $\theta$ as [*Ulaby et al.*, 1986]

$$E(\theta) = 1 - \Gamma(\theta). \quad (3)$$

[33] The term "reflectivity" here is used to denote the total average fraction of incident radiation scattered from the surface into the upper hemisphere (and should not be confused with the Fresnel reflection coefficient $|R(\varepsilon, 0)|^2$). Reflectivity includes both radiation reflected at the upper interface and radiation scattered by the lower interface and transmitted to the upper half-space through the mantle (thin lines in Figure 11). The latter was integrated over all possible scattering angles.

### 3.2. Scattering at the Substrate

[34] To perform calculations with equation (1) through equation (3), we need to know the backscattering coefficient at the mantle-substrate interface $S(\varepsilon_{12}, \xi, \theta')$ and also the bidirectional reflection coefficient at the same surface to calculate $\Gamma(\theta)$.

[35] The average backscatter of the surface of Venus as a function of incidence angle is known to fit Hagfors law [*Hagfors*, 1970] for incidence angles <15°, and the Muhle-

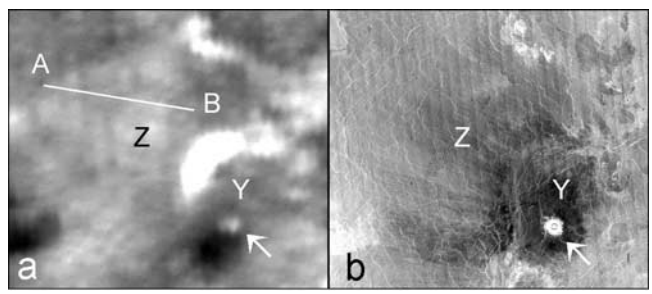


**Figure 7.** Emissivity feature of the N type associated with the crater Comnena (1.2°S, 343.7°E, 19.0 km). (a) Emissivity map. The length of segment AB is 250 km. (b) SAR image.

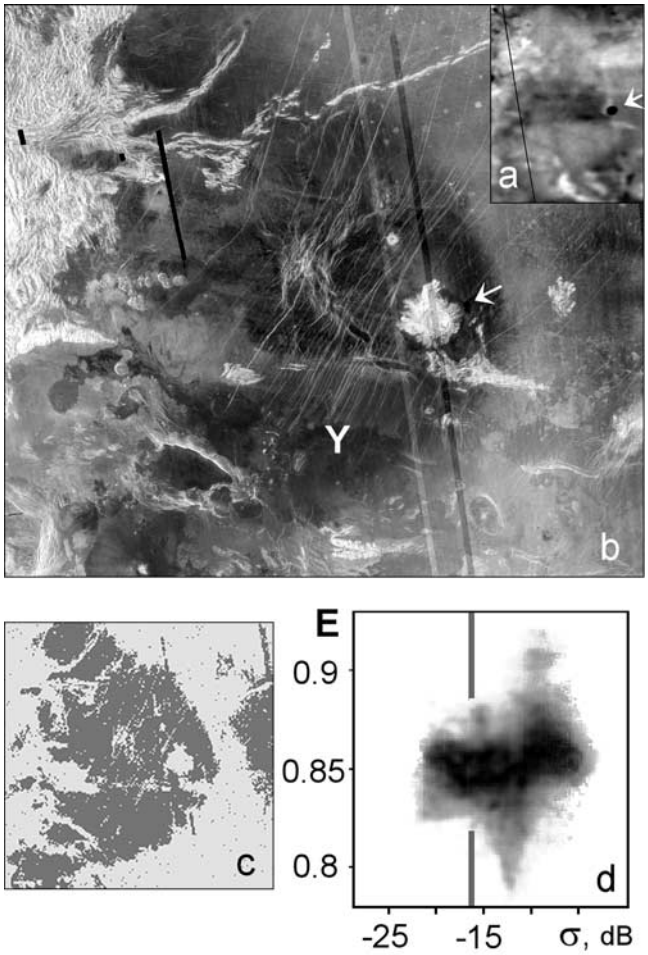


**Figure 8.** Crater Stuart (30.79°S, 20.22°E, 68.6 km). (a) Emissivity map; a BW-type emissivity feature is seen. (b) SAR image. (c) The area formally classified as DDF according to the SAR cross section is shaded. (d) Emissivity ($E$)-radar cross-section ($\sigma$) diagram; vertical line denotes the threshold used for classification in Figure 8c.

man law [*Muhleman*, 1964] in the 20°–60° range of incidence angles. Muhleman and Hagfors laws were derived on the basis of the supposition that the surface can be considered as representing a Gaussian random process with different autocorrelation functions. During the Pioneer-Venus mission [*Pettengill et al.*, 1988] parameters of the Muhleman law were revised using the median backscattering function related mostly to the Venus plains. This law does not refer to the permittivity of the scattering surface.

[36] Microwave scattering by rough surfaces is often described as a combination of (1) quasi-specular scattering depending on larger-scale surface roughness and dominating at low incidence angles and (2) diffuse-like scattering depending on smaller-scale roughness and dominating at larger incidence angles. Models based on this approach were used to study backscattering by *Pettengill et al.* [1988], *Campbell et al.* [1992], and *Campbell* [1994]. Such models are complex and contain many poorly constrained parameters. We decided not to use such rigorous scattering models. Instead, we applied an heuristic approach which allowed us to recalculate the scattering coefficient for a pure surface $S(\varepsilon_1, \xi, \theta)$ into a backscattering and bidirectional scattering coefficient at the mantling substrate interface.

[37] We formally consider a model surface that has larger-scale surface roughness only. Scattering of the model surface can be modeled with the Kirchhoff method. We choose the model surface so that the pure surface exhibits both radar cross section and emissivity equal to the observed values. In the frame of the Kirchhoff method, the backscattering and bidirectional scattering coefficients can be expressed through the slope-frequency distribution of the surface tilts. In particular, for the backscattering

$$S(\varepsilon, \xi, \theta) = \frac{|R(\varepsilon, 0)|^2}{2\cos\theta} p(\theta, \xi), \tag{4}$$

where $p(\theta, \xi)$ is the properly normalized slope-frequency distribution density. To calculate the bidirectional scattering coefficient we used the "stationary phase approximation" model described in detail by *Ulaby et al.* [1986]. In particular, this approximation takes into account the depolarization effect.

[38] We chose the slope-frequency distribution for the model surface consisting of small-tilt and large-tilt parts, which reflects the quasi-specular nature of the reflection:

$$p(\theta, \xi) = \begin{cases} K \cdot G(\theta, \xi_S), & 0 < \theta < 12^\circ \\ G(\theta, \xi), & \theta > 12^\circ \end{cases}, \tag{5}$$

where

$$G(\theta, \xi) = \frac{\exp\left(-\tan^2\theta / 2\xi^2\right)}{\xi^2 \cos^3\theta}. \tag{6}$$

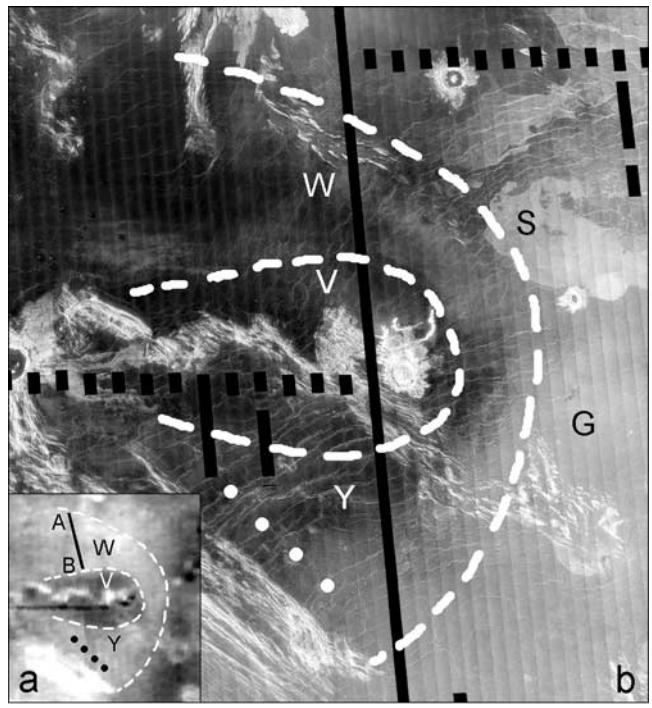


**Figure 9.** Crater Ban Zhao (17.2°N, 146.9°E, 38.3 km) with dark parabola. (a) Emissivity. The length of segment AB is 170 km. (b) SAR image ($\sigma$) for the same region.

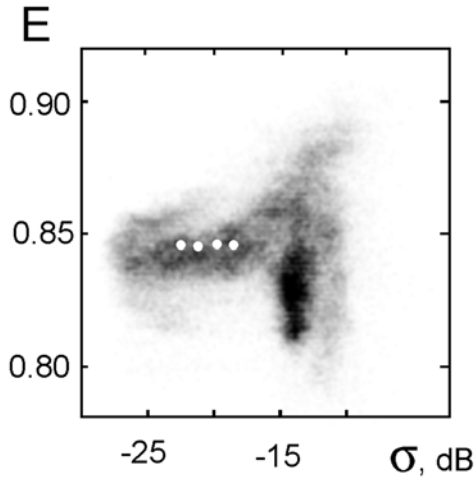


**Figure 10.** Emissivity ($E$)-radar cross-section ($\sigma$) diagram for the crater Ban Zhao (Figure 9) and the location of surface points marked with dots in Figure 9 in the $\sigma$-$E$ domain.

Coefficient $K$ in equation (5) was chosen to provide the proper normalization [*Tyler et al.*, 1992] of the distribution density for given parameters $\xi$ and $\xi_S$. Parameters $\xi$ and $\xi_S$ represent the characteristic slopes of the small-tilt and large-tilt parts of the model surface. From the Magellan altimeter experiment, Venus plains are known to be characterized by mean slopes from 2.5° to 4° at 0–10° incidence angles [*Ford and Pettengill*, 1992]. We chose $\xi_S = 3°$. The model results are not sensitive to variations of this parameter over a rather wide range.

[39] Finally, we chose parameters $\varepsilon$ and $\xi$ to fit the observed emissivity and radar cross section for a "clear" surface close to the DDF and geologically similar to the DDF substrate with modeled emissivity and radar cross section. The later is simply obtained from equation (4), while calculation of modeled emissivity demanded integration over all scattering angles. With $\varepsilon$ and $\xi$ chosen, the slope-frequency distribution is defined, and the backscattering and bidirectional scattering coefficients at the mantle-substrate interface can be calculated, which allowed us to calculate the radar cross section and emissivity for the model with the mantle.

[40] Although the choice of the slope-frequency distribution function (equation (5)) looks rather arbitrary, it gives consistent results. For typical radar cross section and emissivity, the derived roughness parameter $\xi$ provides good agreement with the model backscattering function for a pure surface with the observed average Venus backscattering function [*Pettengill et al.*, 1988] in the range of incidence angles from 20 to 45°. The Fresnel reflection coefficient for the derived $\varepsilon$ turned out to be always close to that derived from the radar altimeter data [*Ford and Pettengill*, 1992].

### 3.3. Model Calculations

[41] The emissivity-radar cross-section diagram with some results of the model calculations using equation (2) and equation (3) are presented in Figure 12. The calculations were made for a parameter set typical for the crater Ban Zhao site (Figure 9). The incidence angle was $\theta$ =

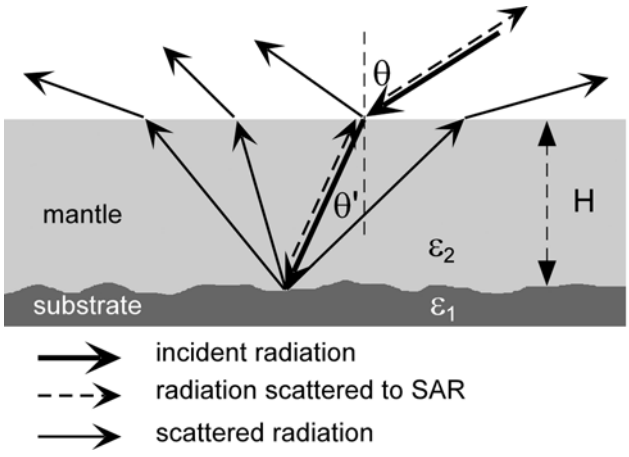


**Figure 11.** Diagram illustrating the model for microwave properties of mantled surfaces. Substrate permittivity is $\varepsilon_1$, mantle permittivity is $\varepsilon_2$, and mantle thickness is $H$. The path of the incident radiation is marked with a thick solid line. The backscatter path is marked with a dashed line. Paths of radiation included in the calculation of emissivity are marked with thin lines.

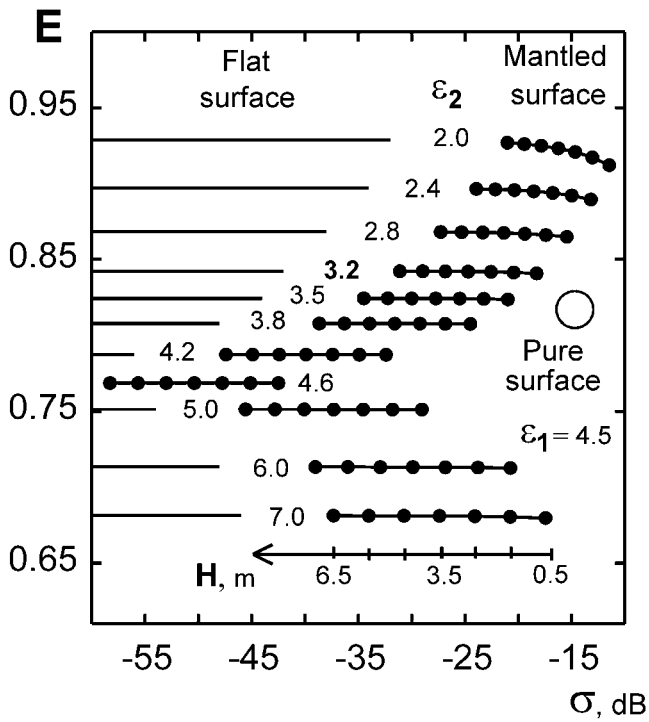


**Figure 12.** Example of model results. Emissivity $E$ and radar cross section $\sigma$ at incident angle $\theta = 44.8°$ for the surface with structure shown in Figure 11. The dielectric permittivity of the mantle $\varepsilon_2$ varies from 2.0 to 7.0. The mantle thickness $H$ varies from 0.5 m to 6.5 m, and the dielectric permittivity of the substrate $\varepsilon_1 = 4.5$. The open circle corresponds to the surface without a mantle. Thin lines in the left side of the plot are represented emissivity level from flat surfaces of corresponding permittivity.

44.8°. The dielectric permittivity of apparently pure surface units surrounding the crater derived through radar cross-section and emissivity measurement varies from 4.2 to 5.2. For the calculations, a substrate permittivity of 4.5 was used. Figure 12 shows the calculated observable characteristics for a range of mantle material permittivity (from 2.0 to 7.0) and depth (from 0.5 m up to 6.5 m). The loss tangent of mantle material was $\tan\Delta = 0.003$.

[42] The circle in Figure 12 shows the location of the surface without mantle in the radar cross-section–emissivity domain. The presence of the mantle shifts the observed values of radar cross section and emissivity compared to the pure surface. For a constant mantle thickness, an increase of mantle permittivity causes a decrease of emissivity. However, the difference in radar cross section is controlled mainly by the difference in permittivity between substrate and mantle materials. Low differences in permittivity cause very low radar cross section and cause the mantled surface to be similar to a pure flat surface. Pure substrate looks identical in radar cross section to the mantled surface when mantle permittivity is 2.6 and mantle depth is 50 cm. However, emissivity for the mantled surface is higher.

[43] An increase in mantle thickness causes a decrease in observed radar cross section (Figure 12). The radar cross section drops by about 13 dB when the mantle thickness increases from 0.5 m to 6.5 m (Figure 12). This decrease depends on the mantle permittivity that determines the angle of refraction at the upper interface, and on the whole path of the radiation in the mantle. Emissivity depends weakly on the mantle thickness. Surfaces with mantles of 0.5 m to 6.5 m deep differ from each other by only 0.1%. This difference is much smaller than the precision of Magellan emissivity measurements [*Pettengill et al.*, 1992]. The emissivity for every mantled surface (Figure 12) is close to that of the upper flat interface. The emissivity of a thick mantle without any substrate is shown in Figure 12 as thin horizontal lines for each permittivity value.

[44] The emissivity of the mantled surface, as shown in Figure 12, is mostly sensitive to the dielectric permittivity of the mantles. The backscatter coefficient of the mantled surface is mostly sensitive to mantle thickness. With the accuracy of the Magellan emissivity data, the emissivity of the mantled surface can be considered equal to the one from the upper flat interface.

[45] Comparison between the observations (Figure 10) and the model (Figure 12) shows the similarities of general behavior. It suggests that the proposed model is adequate for the description of mantled surfaces exhibiting BW (black and white type) high-emissivity features. The high-emissivity feature of the crater Ban Zhao (Figure 9) is formed by material with a permittivity of $\varepsilon_2 = 3.2$. The gradual darkening of radar brightness toward the parabola (Figure 9) is caused by the increase of mantle thickness up to about 3 m (if $\tan\Delta = 0.003$).

[46] For this value of $\varepsilon_2$, the radiation reaches the substrate at an angle of $\theta' = 23.2°$. The angle of total reflection is 34° and only scattering angles from the substrate in the range 0–34° contribute to the emissivity calculations.

[47] Mantles usually cover large areas that can be composed of many different terrain types and geological materials and units. We used the model to study the sensitivity of observable properties to changes in substrate properties. Again, we used the viewing geometry and physical characteristics typical of the crater Ban Zhao site.

[48] The decrease in the substrate permittivity $\varepsilon_1$ from 4.5 to 3.5 causes a decrease in the radar cross section of 11.5 dB; an increase of $\varepsilon_1$ from 4.5 to 5.5 leads to a 4 dB increase in the radar cross section. These results are valid for the whole range of mantle depths. The emissivity of a thick mantle does not change when the substrate permittivity varies; for a 50 cm thick mantle the emissivity variations are below 0.4% for $\varepsilon_1$ within the 3.5–5.5 range.

[49] Steeper surface slopes cause higher radar cross sections. The change of parameter $\xi$ in the range of ±0.09 leads to variations of radar brightness in the range of ±0.5 dB and to an emissivity change smaller than 0.1%.

[50] For the eastern and central parts of BW-type parabolas, we saw a gradual increase of radar brightness from the center to the margins of the feature. We showed that this could be caused by a systematic decrease of mantle thickness toward the margins. The structure of mantled surfaces in the inner and western parts of parabola features is more complex.

## 4. Thick and Thin Mantles

[51] A very thick mantle would cause a high absorption of radiation during its passage through the mantle to the substrate and back. This leads to the condition that the substrate would not be visible through the mantle. The emissivity for such a surface would be determined by the upper interface, and the backscattering cross section would fall to zero. Very low radar cross sections, however, are not observed on the surface of Venus. Even for the darkest parts of the DDF the measured radar cross section is usually above the noise. There are several reasons for this.

[52] First, the absorption in the mantle material could never be high enough to hide the substrate. According to equation (1), this holds when all three of the permittivity, the loss tangent, and the mantle thickness values are not too high. From cratering mechanics [*Vervack and Melosh*, 1992], the crater-related deposits were shown to be several meters thick. If mantle physical properties are not unusual, the mantles would be partly transparent. Second, the upper mantle surface is unlikely to be exactly flat due to modification processes that can roughen the surface.

[53] The case of thin mantles formally comes out of the limits of validity of ray optics. The lower limit of mantle thickness, above which the diffraction effects can still average out, is the wavelength of radiation in the mantle material. When mantle permittivity is $\varepsilon_m$ the wavelength of radiation $\lambda_m$ inside the mantle is $\lambda_m = \lambda/\sqrt{\varepsilon_m}$, where $\lambda$ is the wavelength in free space. In the Magellan experiment $\lambda = 12.6$ cm and, for example, for mantles with permittivity of 3.2 (as in the case of the crater Ban Zhao) the lower limit is equal to 7 cm. For a mantle permittivity of 4.4, as is the case for some mantles at the crater Carson (24.2°S, 344.1°E, 37.6 km), the lower limit decreases down to 6 cm.

[54] A mantle thickness of 6–7 cm becomes comparable to the vertical roughness scale, which for terrestrial analogs varies over the 2–10 cm range [*Shepard et al.*, 2001]. In Venera 9, 10, 13, and 14 panoramas the surface shows

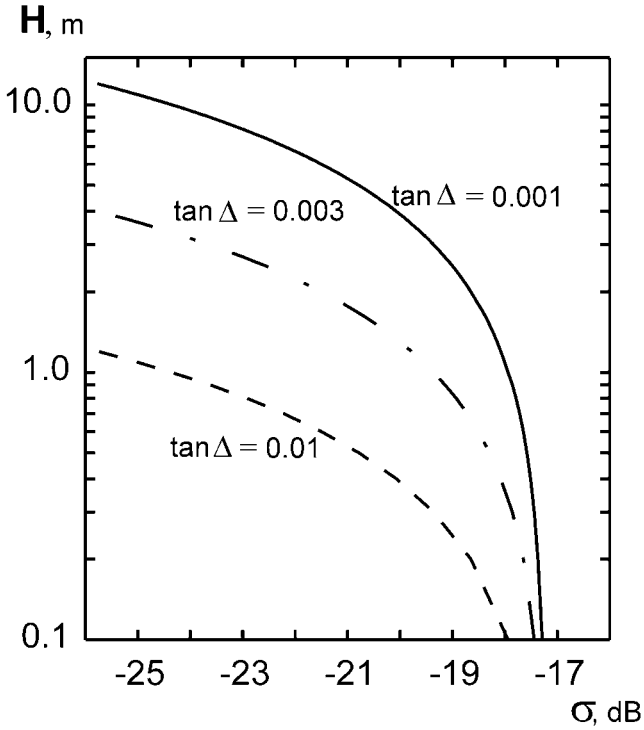


**Figure 13.** The dependence of inferred mantle depth $H$ on radar cross section $\sigma$ for loss tangent values of 0.001, 0.003, and 0.01. The section corresponds to the section marked with dots in Figure 9b for the crater Ban Zhao extended to the boundaries of the high-emissivity feature.

comparable topography [*Florensky et al.*, 1977; *Basilevsky et al.*, 1985]. Loose material could fill depressions (smaller then the spatial resolution of radar images) and cause partial radar darkening. It seems probable that the surface would be a combination of patches of relatively thick mantle (so the model is applicable) and unmantled surface. The emissivity of a partly mantled surface would depend on the proportion of mantled areas.

[55] If the mantle is thin but not patchy, the emissivity would have some intermediate value between that of a pure surface and of that of a flat thick mantle. Such a situation could occur for the site Z located inside the DDF of the crater Nadine (Figure 5).

[56] The path of the radiation through the mantle depends on the incidence angle. Equatorial regions of the surface of Venus were observed with shallower incidence (i.e., higher incidence angles), and the whole path of radiation in the mantle was longer compared to higher latitudes. This means that the mantles in the low-latitude zones should be more pronounced in the SAR images than at higher latitudes. This explains the observation by *Basilevsky and Head* [2002a] that the total number of dark-parabola craters in the low-latitude zone (steep incidence angles) is greater than that of the high-latitude zones.

[57] When the mantle layer is thin, the absorption of radiation does not play an important role. In Figure 13, estimates of mantle depths along a line marked with dots in Figure 9 are shown as a function of radar cross section for three values of mantle loss tangent. In the inner part of the parabola, the thickness is very sensitive to the assumed loss tangent. But in the outer part of parabolas, the mantle thins to $\sim$10 cm at every loss tangent value. The difference between pure and mantled surfaces in this case is not seen distinctly in SAR images. This explains the extended crater-related deposits that are not seen in SAR images but are seen as low-emissivity parabolas. For the crater Nadine (Figure 5), the DDF material is thinner than the mantle for crater Li Quingzhao (Table 4).

## 5. Results and Discussion

[58] We mentioned above that the emissivity of the mantled surface is almost equal to the one defined by the Fresnel reflection coefficient at the upper flat interface. This means that the derived $\varepsilon_2$ estimates are not sensitive to the particular choice of the slope-frequency distribution for the model substrate. This choice, however, can bias somewhat the derived estimates of the mantle thickness.

[59] We assumed a homogeneous mantle with a flat upper surface. There are many examples where lava flow boundaries can be traced inside DDF in the radar images [see, e.g., *Campbell et al.*, 1992]. This indicates that the scattering at the upper mantle surface and volume scattering inside the

**Table 4.** Estimates of Mantle Depths for Selected Sites

| | | Mantle Depth, m | | |
|---|---|---|---|---|
| Crater | Site | tanΔ = 0.001 | tanΔ = 0.003 | tanΔ = 0.005 |
| Faustina (Figure 2) | Y | 18.5 | 6.1 | 3.7 |
| Faustina (Figure 2) | Z | 17.2 | 5.8 | 3.5 |
| Faustina (Figure 2) | W | 4.5 | 1.6 | 0.9 |
| Sitwell (Figure 3) | Y | 4.0 | 1.2 | 0.7 |
| Sitwell (Figure 3) | B | 9.0 | 3.0 | 1.8 |
| Li Quingzhao (Figure 4) | Y | 3.8 | 1.3 | 0.8 |
| Li Quingzhao (Figure 4) | W | 3.75 | 1.25 | 0.75 |
| Nadine (Figure 5) | Y | 1.3 | 0.45 | 0.25 |
| Nadine (Figure 5) | X | 0.45 | 0.2 | 0.1 |
| Nadine (Figure 5) | W | 4.5 | 1.5 | 0.9 |
| Unnamed (Figure 6) | Y | 1.5 | 0.5 | 0.25 |
| Comnena (Figure 7) | Y | 5.5 | 1.9 | 1.15 |
| Comnena (Figure 7) | Z | 3.2 | 1.1 | 0.65 |
| Stuart (Figure 8) | Y | 6.3 | 2.1 | 1.25 |
| Ban Zhao (Figure 9) | Y | 13.6 | 4.5 | 2.7 |
| Ban Zhao (Figure 9) | V | 8.6 | 2.6 | 1.8 |

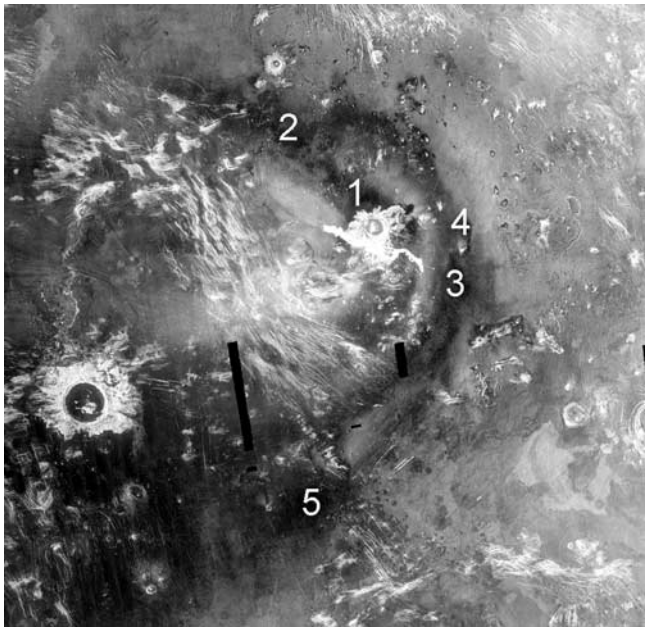


**Figure 14.** Magellan SAR image of the crater Carson (24.2°S, 344.1°E, 37.6 km).

mantle are small enough, and the radar does "see" the rough mantle-substrate interface.

[60] Estimated mantle thickness for several sites in DDF areas (Figures 2–9) are shown in Table 4 for four values of mantle loss tangent. The mantle in the northern and southern parts of the high-emissivity feature associated with the crater Faustina (Figure 2b, sites Y and Z, respectively) is similar in thickness and thicker than in site W inside the low-emissivity feature. The reverse situation is observed for the crater Sitwell (Figure 3): the high-emissivity parabola in site Y is thinner then the low-emissivity parabola in the site B.

[61] The mantle thickness for the crater Li Quingzhao (Figure 4) at sites Y and W is almost the same. The two sites show two different subunits composing the parabola. In the western part of the parabola, the radar cross section differs by about 2 dB from those of sites Y and W. This translates into differences in mantle thickness in the range of about 0.5 m ($\tan\Delta = 0.003$). Thus the radar cross-section decrease in this area is caused by the presence of the mantle. The western part of the parabola of the crater Li Quingzhao is described as a lobate flow by *Ivanov and Head* [2001]. The mantle here is possibly thin enough to allow the tracing of a geological boundary.

[62] The crater Nadine (Figure 5) does not differ in size from the crater Li Quingzhao (Figure 4) but exhibits only a weak radar feature not seen as a parabola. The darkest area in Figure 5b (site W) corresponds to the thickest mantle and is thicker than the mantle for crater Li Quingzhao. Other sites inside the Nadine emissivity parabola (Figures 5a and 5b, sites X and Y) are characterized by a thin mantle down to ~20 cm ($\tan\Delta = 0.003$). As a whole, mantles over the emissivity parabola area of the crater Nadine are thinner than the one for the crater Li Quingzhao.

[63] The radar-dark parabola of the crater Comnena (Figures 7a and 7b) is characterized by a large emissivity feature in the western part. Deposits in this area appear similar to wind streaks. Their rather uniform emissivity in the area points to the presence of mantles with similar physical properties but variable depths. At point Z inside the area (Figure 7b) the mantle depth is ~1.1 m ($\tan\Delta = 0.003$).

[64] The prediction of mantle thickness strongly depends on assumptions about the loss tangent value. We tried to constrain the choice of loss tangent value by using some independent estimates. Specifically, we considered the calculations of the amount of loose material deposited from the model of *Vervack and Melosh* [1992] for the crater Carson (24.2°S, 344.1°E, 37.6 km) shown in Figure 14. The crater has a BW (black and white) type emissivity feature (Table 1). The possible mantle thicknesses in locations marked with 1 through 5 in Figure 14 for eight loss tangent values are presented in Table 5. For comparison, these data are shown with the depth reported by *Vervack and Melosh* [1992] in approximately the same locations. The shape of the parabola obtained by *Vervack and Melosh* [1992] is symmetric. Among the sites chosen, the lowest radar cross section occurs near the location of the thickest mantle estimated by *Vervack and Melosh* [1992]. The mantle depths predicted from cratering mechanics and derived from electromagnetic properties approximately coincide for $0.001 < \tan\Delta \leq 0.005$. These values are similar to those obtained for a variety of dry powdered terrestrial rock samples [*Campbell and Ulrichs*, 1969].

[65] Classification of emissivity features shows some trend with regard to crater size. BW (black and white) type emissivity features are observed only for craters with diameters >22 km (Table 1). Pure parabolic features (P-type) are observed only for crater diameters <28 km (Table 2). PW emissivity type features (parabola-white) are seen for craters between ~12–38 km diameter (Table 1). N-type features are observed over a wide range of crater diameters, from ~10–50 km (Table 3). Six craters from this subset are located in very rough terrains, and the absence of emissivity features may be not apparent due to complex surroundings.

[66] The decrease in radar cross section in the parabola population is higher for BW-type craters (7.2–12.8 dB) compared to PW-type (4–10.4 dB) and P-type craters (2.6–9.2 dB). The radar contrast does not show an obvious dependence on crater size. For example, a decrease in radar brightness by 4 dB occurs for the P-type crater Rovena (with a diameter of 19.6 km), for an unnamed crater (with a diameter of 9.4 km) (Table 2), and for a PW unnamed crater (with a diameter 12.8 km) (Table 1).

**Table 5.** Mantle Depths for Selected Sites in the DDF of Crater Carson

| | Model Mantle Depth, m | | | | |
|---|---|---|---|---|---|
| $\tan\Delta$ | Site 1 | Site 2 | Site 3 | Site 4 | Site 5 |
| 0.001 | 1.5 | 4.1 | 6.0 | 5.9 | 7.4 |
| 0.002 | 0.8 | 2.0 | 3.0 | 2.9 | 3.7 |
| 0.003 | 0.5 | 1.4 | 2.0 | 1.9 | 2.5 |
| 0.004 | 0.4 | 1.0 | 1.5 | 1.4 | 1.85 |
| 0.005 | 0.3 | 0.8 | 1.2 | 1.1 | 1.5 |
| 0.006 | 0.25 | 0.75 | 1.0 | 0.9 | 1.25 |
| 0.007 | 0.23 | 0.6 | 0.85 | 0.8 | 1.05 |
| 0.008 | 0.2 | 0.5 | 0.75 | 0.7 | 0.9 |
| Mantle depth[a] | 0.5 ~ 1 | >1 | >1 | >1 | >1 |

[a]From [*Vervack and Melosh*, 1992].

[67] For craters in the 22–38 km diameter range, the sequence of emissivity feature types is accompanied by a decrease in radar cross-section contrast from 8–12.8 dB for the BW type, through 8–10.2 dB for the PW type, to 2.6–9.2 dB for the P type. This can be interpreted as representing an increase in parabola age. N-type craters can either represent a subsequent step in parabola degradation or simply result from a complex environment hiding or obscuring the emissivity feature.

[68] The observed difference in emissivity features related to small (D < 22 km) and large (D > 38 km) craters points to a difference in the processes associated with mantle formation and/or differences in the nature of the mantle material. The latter could be caused by the systematic difference in the depth of excavation.

[69] High-emissivity features of the BW type correspond to mantles with uniform permittivity over large areas. Hence each of these mantles is probably formed by material of equal porosity and therefore is composed of either well-sorted or well-mixed particles.

[70] Particle sorting can occur during ejecta transport through the atmosphere [*Vervack and Melosh*, 1992; *Campbell et al.*, 1992]. Coarse particles land first. Dense packing of mantle could be caused by the influence of winds at the surface on the landing particles. Winds at 1 m heights can reach 1.2 m/s as in Venera −9 and −11 landing sites [*Avdievsky et al.*, 1976]. Fine particles moved laterally by winds can compactly fill gaps between coarser particles that have previously landed. Low-emissivity areas in the BW type features may indicate the presence of such a low-porosity deposit of coarse and fine particles, whose dielectric permittivity approaches that of solid rock.

## 6. Conclusions

[71] This analysis of radar-dark parabolas incorporating emissivity data revealed that DDF-like crater-related deposits have a much wider extent then dark areas seen in SAR images alone. The presence of the mantle strongly influences the observed scattering and emission properties. Estimates of mantle depths for several craters were obtained using Magellan radiometric and radar data with a model for the microwave properties of mantled surfaces. Mantle thickness varies from about 10 cm to several meters, assuming a loss tangent of $\tan\Delta = 0.003$. Thin deposits down to 7 cm can form emissivity parabolas not seen in SAR images.

[72] A loss tangent of mantle material lower then 0.005 but higher then 0.001 is in good agreement with the distribution of mantle thickness for the crater Carson as modeled by *Vervack and Melosh* [1992].

[73] Four types of emissivity features associated with radar-dark parabolas were classified and described. The distribution of craters of the emissivity feature types point to different styles of ejecta deposition for large (diameter > 38 km) and small (diameter < 22 km) craters. The differences in emissivity types for craters in the 22–38 km diameters range can be treated as the differences in the degradation state of mantle material.

[74] These results provide a basis for the interpretation of the character and thickness of mantle deposits, their states of degradation, processes associated with their formation and degradation, and guides to their use in establishing stratigraphic relationships and ages of underlying geologic units on Venus. The results will also be useful in interpreting the nature of surface deposits at previous landing sites and predicting the nature of deposits likely to be encountered at future landing sites.

[75] **Acknowledgments.** The authors thank M. A. Kreslavsky, A. T Basilevsky, and M. A. Ivanov for useful discussions. The authors thank P. Ford and an anonymous reviewer for thoughtful comments that helped to improve the paper.

## References

Arvidson, R. E., V. R. Baker, C. Elachi, R. S. Saunders, and J. A. Wood (1991), Magellan: Initial analysis of Venus surface modification, *Science*, *252*, 270–276.

Arvidson, R. E., R. Greeley, M. C. Malin, R. S. Saunders, N. Izenberg, J. J. Plaut, E. R. Stofan, and M. K. Shepard (1992), Surface modification of Venus as inferred from Magellan observations of plains, *J. Geophys. Res.*, *97*, 13,303–13,317.

Avdievsky, V. S., et al. (1976), Measurement of wind velocity on the surface of Venus during the operation of stations Venera 9 and Venera 10, *Cosmic Res.*, Engl. Transl., *14*, 622–625.

Basilevsky, A. T., and J. W. Head (1995), Regional and global stratigraphy of Venus: A preliminary assessment and implications for the geological history of Venus, *Planet. Space Sci.*, *43*, 1523–1553.

Basilevsky, A. T., and J. W. Head (1998), The geologic history of Venus: A stratigraphic view, *J. Geophys. Res.*, *103*, 8531–8544.

Basilevsky, A. T., and J. W. Head (2000), Geologic units on Venus: Evidence for their global correlation, *Planet. Space Sci.*, *48*, 75–111.

Basilevsky, A. T., and J. W. Head (2002a), Venus: Analysis of the degree of impact crater deposit degradation and assessment of its use for dating geological units and features, *J. Geophys. Res.*, *107*(E8), 5061, doi:10.1029/2001JE001584.

Basilevsky, A. T., and J. W. Head III (2002b), On rates and styles of late volcanism and rifting on Venus, *J. Geophys. Res.*, *107*(E6), 5041, doi:10.1029/2000JE001471.

Basilevsky, A. T., R. O. Kuzmin, O. V. Nikolaeva, A. A. Pronin, L. B. Ronka, V. S. Avduevsky, G. R. Uspensky, Z. P. Cheremukhina, V. V. Semenchenko, and V. M. Ladygin (1985), The surface of Venus as revealed by the Venera landings: Part II, *Geol. Soc. Am. Bull.*, *96*, 137–144.

Basilevsky, A. T., J. W. Head, and I. V. Setyaeva (2003), Venus: Estimation of age of impact craters on the basis of degree of preservation of associated radar-dark deposits, *Geophys. Res. Lett.*, *30*(18), 1950, doi:10.1029/2003GL017504.

Born, M., and E. Wolf (1964), *Principles of Optics*, 808 pp., Pergamon, New York.

Campbell, B. A. (1994), Merging Magellan emissivity and SAR data for analysis of Venus surface dielectric properties, *Icarus*, *112*, 187–203.

Campbell, D. B., N. J. S. Stacy, W. I. Newman, R. E. Arvidson, E. M. Jones, G. S. Musser, A. Y. Roper, and C. Schaller (1992), Magellan observations of extended impact crater related features on the surface of Venus, *J. Geophys. Res.*, *97*, 16,249–16,277.

Campbell, M. J., and J. Ulrichs (1969), Electrical properties of rocks and their significance for lunar radar observations, *J. Geophys. Res.*, *74*, 5867–5881.

Carter, L. M., D. B. Campbell, and B. A. Campbell (2004), Impact crater related surficial deposits on Venus: Multipolarization radar observations with Arecibo, *J. Geophys. Res.*, *109*, E06009, doi:10.1029/2003JE002227.

Florensky, K. P., L. B. Ronka, A. T. Basilevsky, G. A. Burba, O. V. Nikolaeva, A. A. Pronin, A. M. Trakhtman, V. P. Volkov, and V. V. Zazetsky (1977), The surface of Venus as revealed by Soviet Venera 9 and 10, *Geol. Soc. Am. Bull.*, *88*, 1537–1545.

Ford, J. P., and J. J. Plaut (1993), Magellan image data, in *Guide to Magellan Image Interpretation*, pp. 7–18, Jet Propul. Lab., Pasadena, Calif.

Ford, P. G., and G. H. Pettengill (1992), Venus topography and kilometer-scale slopes, *J. Geophys. Res.*, *97*, 13,103–13,115.

Greeley, R., R. E. Arvidson, C. Elachi, M. A. Geringer, J. J. Plaut, R. S. Saunders, G. Schubert, E. R. Stofan, E. J. P. Thouvenot, and S. D. Wall (1992), Aeolian features on Venus: Preliminary Magellan results, *J. Geophys. Res.*, *97*, 13,319–13,345.

Hagfors, T. (1970), Remote probing of the Moon by microwave emissions and by radar, *Radio Sci.*, *5*, 189–227.

Herrick, R. R., and R. J. Phillips (1994), Implications of a global survey of Venusian impact craters, *Icarus*, *111*, 387–416.

Ivanov, M. A., and J. W. Head (2001), Geology of Venus: Mapping of a global geotraverse at 30°N latitude, *J. Geophys. Res.*, *106*, 17,515–17,566.

Izenberg, N. R., R. E. Arvidson, and R. J. Phillips (1994), Impact crater degradation on Venusian plains, *Geophys. Res. Lett.*, *21*, 289–292.
Melosh, H. J. (1989), *Impact Cratering: A Geologic Process*, Oxford Univ. Press, New York.
Muhleman, D. O. (1964), Radar scattering from Venus and Moon, *Astron. J.*, *69*, 34–41.
Pettengill, G. H., P. G. Ford, and B. D. Chapman (1988), Venus: Surface electromagnetic properties, *J. Geophys. Res.*, *93*, 14,881–14,892.
Pettengill, G. H., P. G. Ford, and R. J. Wilt (1992), Venus surface radiothermal emission as observed by Magellan, *J. Geophys. Res.*, *97*, 13,091–13,102.
Plaut, J. J. (1993), The non-SAR experiments, in *Guide to Magellan Image Interpretation*, pp. 19–32, Jet Propul. Lab., Pasadena, Calif.
Schaller, C. J., and H. J. Melosh (1998), Venusian ejecta parabolas: Comparing theory with observations, *Icarus*, *131*, 123–137.
Schultz, P. H. (1992), Atmospheric effect on ejecta emplacement and crater formation on Venus from Magellan, *J. Geophys. Res.*, *97*, 16,183–16,248.
Shepard, M. K., B. A. Campbell, M. H. Bulmer, T. G. Farr, L. R. Gaddis, and J. J. Plaut (2001), The roughness of natural terrain: A planetary and remote sensing perspective, *J. Geophys. Res.*, *106*, 32,777–32,795.
Stratton, J. A. (1947), *Electromagnetic Theory*, 615 pp., John Wiley, New York.
Tyler, G. L., R. A. Simpson, M. J. Maurer, and E. Holmann (1992), Scattering properties of the Venusian surface: Preliminary results from Magellan, *J. Geophys. Res.*, *97*, 13,115–13,139.
Ulaby, F. T., R. K. Moore, and A. K. Fung (1986), *Microwave Remote Sensing: Active and Passive*, Artech House, Norwell, Mass.
Vervack, R. J., Jr., and H. J. Melosh (1992), Wind interaction with falling ejecta: Origin of the parabolic features on Venus, *Geophys. Res. Lett.*, *19*, 525–528.
Wood, J. A. (1997), Rock weathering on the surface of Venus, in *Venus II*, edited by S. W. Bougher, D. M. Hunten, and R. J. Phillips, pp. 637–664, Univ. of Ariz. Press, Tucson.

N. V. Bondarenko, Institute of Radiophysics and Electronics, National Academy of Sciences of the Ukraine, 12 Ak. Proskury, Kharkov 61085, Ukraine. (natasha@mare.geo.brown.edu)

J. W. Head, Department of Geological Sciences, Brown University, Box 1846, Providence, RI 02912, USA. (james_head_III@brown.edu)